Supplementary Information for

Electrically tunable spin-orbit interaction in an InAs nanosheet

Furong Fan[1], Yuanjie Chen[1], Dong Pan[2], Jianhua Zhao[2], and H. Q. Xu[1,3,*]

[1]*Beijing Key Laboratory of Quantum Devices, Key Laboratory for the Physics and Chemistry of Nanodevices and School of Electronics, Peking University, Beijing 100871, China*

[2]*State Key Laboratory of Superlattices and Microstructures, Institute of Semiconductors, Chinese Academy of Sciences, P.O. Box 912, Beijing 100083, China*

[3]*Beijing Academy of Quantum Information Sciences, Beijing 100193, China*

*Corresponding author; email: hqxu@pku.edu.cn

(Date: April 30, 2022)

Contents

In this Supplementary Information, we provide, in Sections I, II, III, IV, and V, additional data for the dual-gate field-effect InAs nanosheet device (i.e., Device 1) studied in the main article. In Section VI, we provide the results of measurements obtained from a similar dual-gate field-effect device (named as Device 2) made from another epitaxially grown InAs nanosheet.

Section I. Carrier density (n), Fermi wavelength (λ_F), and mean free path (L_e) in the InAs nanosheet extracted from the device gate-transfer characteristic measurements

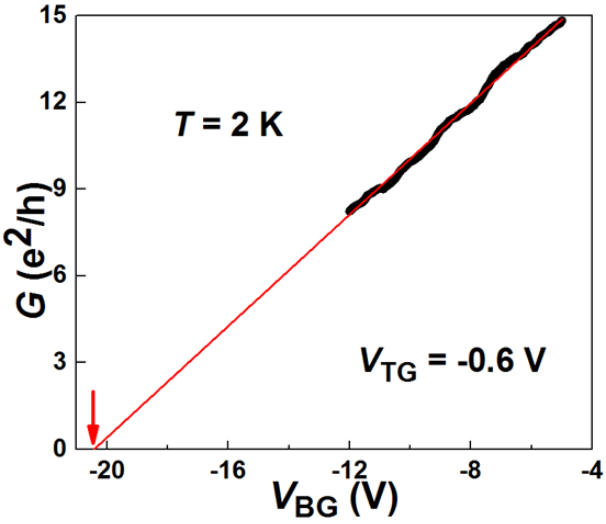

FIG. S1. Conductance G (black line) measured for Device 1 as a function of V_{BG} at fixed V_{TG} = –0.6 V and T = 2 K. The red line is a linear fit to the measured data. The red arrow marks the intersection of the fitting line and the V_{BG} axis, i.e., the bottom-gate threshold voltage of V_{BG}^{th} = –20.2 V at V_{TG} = –0.6 V.

In this Section, we describe how the carrier density (n), Fermi wavelength (λ_F), and mean free path (L_e) in the InAs nanosheet at different conductance values are extracted from the gate-transfer characteristic measurements. The carrier density n in the InAs nanosheet can be estimated from the measured bottom-gate transfer characteristics at a fixed top-gate voltage based on a parallel capacitor model of $n = \frac{C_{BG}\left(V_{BG}-V_{BG}^{th}\right)}{eA}$ with e being the elementary charge, A the area of the InAs nanosheet conduction channel, C_{BG} the bottom-gate capacitance to the nanosheet channel, V_{BG} the applied bottom-gate voltage, and V_{BG}^{th} the bottom-gate threshold voltage at which the nanosheet channel starts to open for conduction. The capacitance C_{BG} can be calculated from $C_{BG} = \frac{\varepsilon_0 \varepsilon_r A}{d}$,

where ε_0 is the permittivity of vacuum, ε_r is the relative permittivity of SiO_2, and d is the thickness of SiO_2. In this work for Device 1, using $\varepsilon_0 \sim 8.85\times10^{-12}$ F/m, $\varepsilon_r \sim 3.9$, $d \sim 200$ nm and $A \sim 0.34$ μm^2, C_{BG} can be estimated out as 5.87×10^{-17} F. The threshold voltage V_{BG}^{th} can be extracted from the fit of the measured $G \sim V_{BG}$ characteristics at a fixed V_{TG} to $G = \frac{\mu}{L^2} C_{BG}\left(V_{BG} - V_{BG}^{th}\right)$, where μ is the field-effect mobility of electrons in the nanosheet. Figure S1 shows the measured $G \sim V_{BG}$ characteristics of Device 1 (black curve) at $V_{TG} = -0.6$ V and $T = 2$ K and the fitting result (red curve). From the fit, a threshold voltage of $V_{BG}^{th} \sim -20.2$ V, as marked by a red arrow in Fig. S1, and a field-effect mobility of $\mu \sim 4460$ cm^2/Vs are extracted. Now, the carrier density n in the InAs nanosheet at different conductance values can be estimated. For example, at the channel conductance of $G \sim 12e^2/h$, the carrier density can be estimated out as $n \sim 1.34\times10^{12}$ cm^{-2} by taking $V_{TG} = -0.6$ V and $V_{BG} = -7.8$ V (cf. the dual-gate transfer characteristic measurements shown in Fig. 2 of the main article and the bottom-gate transfer characteristic measurements shown in Fig. S1). The Fermi wavelength can be estimated from $\lambda_F = \sqrt{2\pi/n}$, giving $\lambda_F \sim 22$ nm at $n \sim 1.34\times10^{12}$ cm^{-2}. The corresponding mean free path in the nanosheet is $L_e \sim 85$ nm, obtained from $L_e = \frac{\hbar\mu}{e}\sqrt{2\pi n}$ (where $\hbar = \frac{h}{2\pi}$ is the reduced Planck constant). Similarly, the values of n, λ_F, and L_e can be extracted from the measured gate-transfer characteristics for the InAs nanosheet at other nanosheet channel conductance values. Table S1 lists the extracted values of n, λ_F, and L_e for the InAs nanosheet in Device 1 at the three channel conductance G values of ~12, ~7 and ~4e^2/h.

TABLE S1. Extracted carrier densities n, Fermi wavelengths λ_F, and mean free paths L_e for the InAs nanosheet in Device 1 at three channel conductance G values of ~12, ~7 and ~4e^2/h.

Conductance G (e^2/h)	Carrier Density n (cm^{-2})	Fermi Wavelength λ_F (nm)	Mean Free Path L_e (nm)
12	1.34×10^{12}	22	85
7	1.07×10^{12}	24	56
4	5.8×10^{11}	33	41

Section II. Tuning of the low-field magnetotransport characteristics of the InAs nanosheet in Device 1 by the bottom and the top gate individually

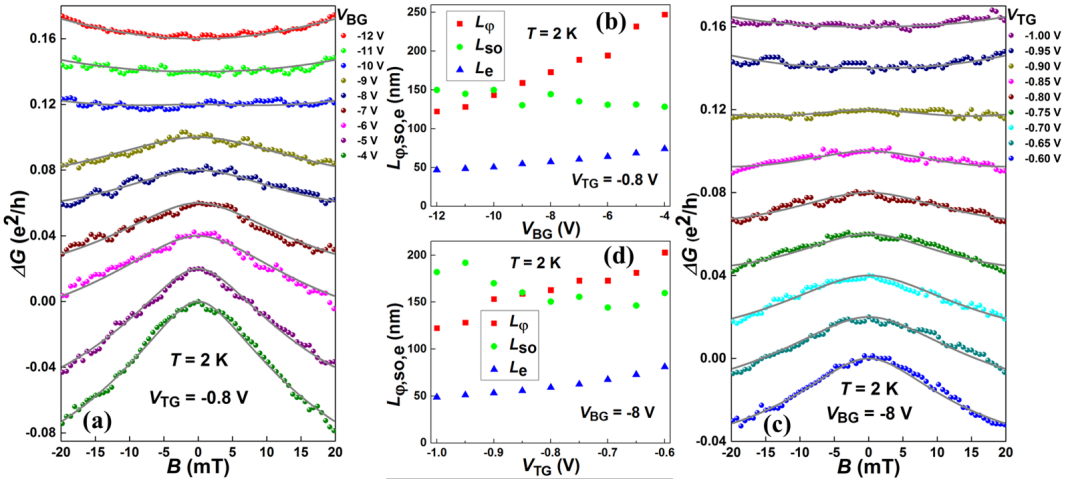

FIG. S2. (a) Low-field magnetoconductance ΔG measured for Device 1 at different V_{BG}, with V_{TG} fixed at V_{TG} = –0.8 V, and at T = 2 K. The bottom green data points display the measured ΔG data at V_{BG} = –4 V and the data points measured at all other values of V_{BG} are successively vertically offset by 0.02e^2/h for clarity. The gray solid lines are the results of the fits of the measured ΔG data to the HLN theory [Eq. (1) in the main article]. (b) Characteristic transport lengths L_φ, L_{SO} and L_e extracted as a function of V_{BG} from the fits shown in (a). (c) Low-field magnetoconductance ΔG measured for Device 1 at different V_{TG}, with V_{BG} fixed at V_{BG} = –8 V, and at T = 2 K. The bottom blue data points display the measured ΔG data at V_{TG} = –0.60 V and the data points measured at all other values of V_{TG} are successively vertically offset by 0.02e^2/h for clarity. The gray solid lines are again the results of the fits of the measured ΔG data to the HLN theory [Eq. (1) in the main article]. (d) Characteristic transport lengths L_φ, L_{SO}, and L_e extracted as a function of V_{TG} from the fits shown in (c).

In this Section, we provide additional measurement data for the influences of the bottom- and top-gate voltages on the low-field magnetotransport characteristics of the InAs nanosheet in Device 1. Figure S2(a) shows the measured low-field magnetoconductance ΔG of Device 1 as a function of bottom-gate voltage V_{BG} at a fixed top-gate voltage of V_{TG} = –0.8 V and at T = 2 K. Figure S2(c) shows the measured ΔG of Device 1 as a function of V_{TG} at fixed V_{BG} = –8 V and at T = 2 K. It is seen that both V_{BG} and V_{TG} can modulate the low-field magnetotransport characteristics of the

InAs nanosheet effectively, turning the electron transport in the InAs nanosheet from the weak localization (WL) regime to the weak antilocalization (WAL) regime. The solid lines in Figs. 2(a) and 2(c) represent the fits of the measurements to the theory of Hikami, Larkin, and Nagaoka (HLN) [i.e., Eq. (1) in the main article]. Figures S2(b) and S2(d) display the extracted values of L_φ, L_{SO}, and L_e from the fits shown in Figs. S2(a) and S2(c), respectively. Here, it is seen that with varying V_{BG} or V_{TG} alone, L_{SO} does not get largely changed, though an effective change in carrier density n (not shown here) and in phase coherence length L_φ can be achieved. In fact, it is the efficient change in phase coherence length L_φ with change in V_{BG} or in V_{TG} that leads to a crossover between L_φ and L_{SO} and thus a transition from the WL to the WAL regime in the electron transport in the InAs nanosheet. The above results provide a clear evidence that it is difficult to efficiently tune the spin-orbit interaction (SOI) in the InAs nanosheet by a single gate. Thus, in the main article, a dual-gate device setup is developed in order to achieve an efficient tuning of the electric field and thus the Rashba SOI in the InAs nanosheet without a change in carrier density.

Section III. Simulations for the energy band diagrams of the HfO_2/InAs/SiO_2 layer structure in Device 1

To get the physical insights into the experimental results presented in the main article, we carry out the simulations for the energy band diagrams of the HfO_2/InAs/SiO_2 layer structure in the studied dual-gate InAs nanosheet device (Device 1). In the simulations, Poisson's equation is solved in compliance with the boundary conditions set by the experiments. The material parameters of HfO_2, InAs, and SiO_2 used in the energy band diagram simulations are given in Table S2. Here, in the simulations, the three layers of HfO_2, InAs, and SiO_2 are assumed to be infinite in the lateral dimensions and thus the electrostatics of the HfO_2/InAs/SiO_2 layered system can be described by an effective one-dimensional Poisson's equation of $\varepsilon\nabla_z^2\varphi(z) = -\rho(z)$, where ε is the dielectric constant of the material, $\varphi(z)$ is the electric potential, and $\rho(z)$ is the charge density. However, the layer thicknesses of HfO_2, InAs, and SiO_2 are taken as 20 nm, 20 nm, and 200 nm, respectively, which are in close correspondence to the structure of Device 1. The charge density $\rho(z)$ is given by $\rho(z) = e[p(z) - n(z) + N_d(z) - N_a(z)]$, where $p(z)$, $n(z)$, $N_d(z)$, and $N_a(z)$ are the hole density, electron density, donor concentration and acceptor concentration, respectively. The energies of the conduction

band minimum $E_C(z)$ and the valence band maximum $E_V(z)$ are given by $E_C(z) = -[e\varphi(z) + \chi]$ and $E_V(z) = -[e\varphi(z) + \chi + E_g]$, where χ and E_g are the electron affinity and bandgap of the material. We require that the electron Fermi level E_F is continuous at the interface of two different materials and that the simulated charge density in the InAs material is equal to the charge density in the InAs nanosheet extracted from the gate transfer characteristic measurements.

TABLE S2. Material parameters of HfO_2, InAs, and SiO_2 employed in the simulations for the energy band diagrams of the HfO_2/InAs/SiO_2 layer structure in Device 1.

Material	Bandgap (eV)	Dielectric Constant (ε_0)	Electron Effective Mass (m_e)	Electron Affinity (eV)
HfO_2	5.8	9.1	0.42	2.8
InAs	0.354	15.15	0.023	4.9
SiO_2	8.95	3.9	0.427	0.75

Figure S3(a) shows the simulated energy band diagram of the HfO_2/InAs/SiO_2 layer structure in Device 1 at $V_{BG} = V_{TG} = 0$ V ($V_D = 0$ V) and Fig. S3(b) is a zoom-in plot of the energy band diagram in the InAs nanosheet. It should be noted that even in the case of $V_{BG} = V_{TG} = 0$ V, the band structure in the InAs nanosheet is asymmetric, leading to a structural asymmetric and thus the presence of a Rashba SOI in the InAs nanosheet.

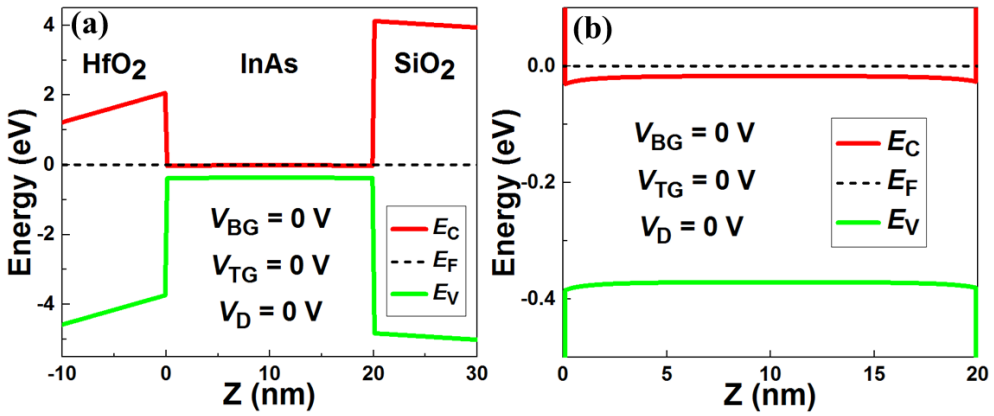

FIG. S3. (a) Simulated energy band diagram of the HfO_2/InAs/SiO_2 layer structure in Device 1 at $V_{BG} = V_{TG} = 0$ V ($V_D = 0$ V). (b) Zoom-in plot of the energy band diagram in the InAs nanosheet.

Section IV. Low-field magnetotransport characteristics measured for Device 1 as a function of dual-gate voltage V_D taken along the constant conductance contours of $G \sim 7e^2/h$ and $G \sim 4e^2/h$

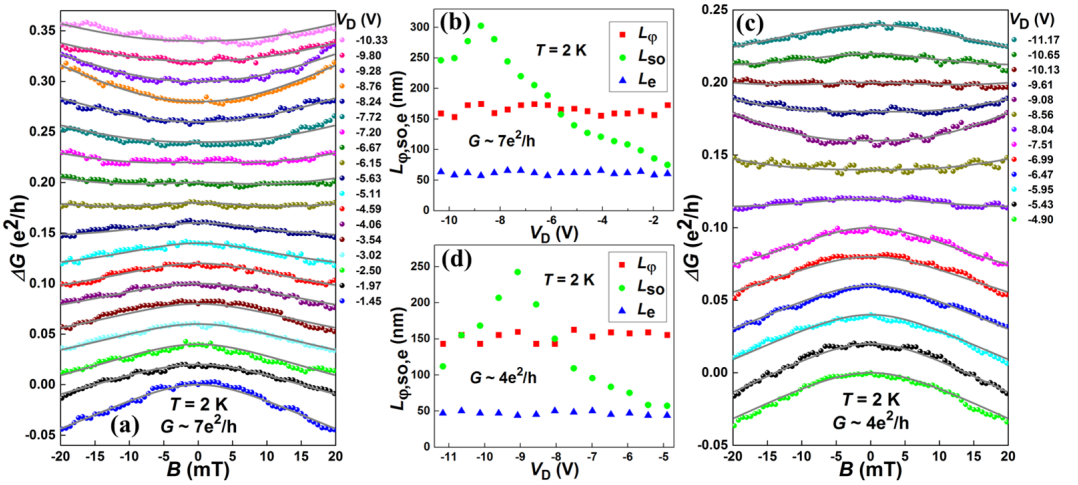

FIG. S4. (a) Low-field magnetoconductance ΔG measured for Device 1 at $T = 2$ K and at a series of dual-gate voltages V_D taken along the constant conductance contour of $G \sim 7e^2/h$. The bottom blue data points display the measured ΔG data at $V_D = -1.45$ V and the ΔG data measured at all other V_D values are successively vertically offset by $0.02e^2/h$ for clarity. The gray solid lines are the results of the fits of the measurements to the HLN theory [Eq. (1) in the main article]. (b) Characteristic transport lengths L_φ, L_{SO}, and L_e as a function of V_D, extracted from the fits in (a). (c) The same as in (a) but for the measurements at different V_D values taken along the constant conductance contour of $G \sim 4e^2/h$. The bottom green data points display the measured ΔG data at $V_D = -4.90$ V and the ΔG data measured at all other V_D values are successively vertically offset by $0.02e^2/h$ for clarity. Again, the gray solid lines are the results of the fits of the measurements to the HLN theory [Eq. (1) in the main article]. (d) Characteristic transport lengths L_φ, L_{SO}, and L_e as a function of V_D, extracted from the fits in (c).

In this section, we provide additional data measured for the low-field magnetotransport characteristics of Device 1 at the constant conductance values of ~7 and ~$4e^2/h$. Figures S4(a) and S4(c) show the low-field magnetoconductance ΔG measured for Device 1 at T=2 K as a function of dual-gate voltage V_D taken along the constant conductance contours of $G \sim 7e^2/h$ and $G \sim 4e^2/h$, respectively. The solid lines in the figures are the results of the fits of the measurement data to the HLN theory [Eq.

(1) in the main article]. Figures S4(b) and S4(d) show the extracted characteristic transport lengths L_φ, L_{SO} and L_e from the fits shown in Figs. S4(a) and S4(c), respectively. Here, both L_φ and L_e are seen to show a weak dependence on V_D. However, with decreasing V_D, the extracted L_{SO} undergoes a dramatic change—it first increases quickly and then falls down. This efficient modulation of L_{SO} in the InAs nanosheet at different constant carrier densities (revealed by staying at different constant conductance values) by dual-gate voltage V_D reveals again that an SOI of the Rashba type is present in the InAs nanosheet and is greatly tunable with use of the dual gate, in full consistence with the results presented in the main article.

Section V. Rashba spin-orbit coupling constant α and its extraction for the InAs nanosheet in Device 1 at the conductance values of $G \sim 7e^2/h$ and $\sim 4e^2/h$.

We have extracted the spin-orbit lengths L_{SO} in the InAs nanosheet of Device 1 at three fixed conductance values of G~$12e^2/h$, ~$7e^2/h$ and ~$4e^2/h$ from the low-field magnetotransport measurements shown in Figs. 3 and S4. The efficient tuning of L_{SO} at a constant conductance with use of the dual gate demonstrates that the tuned SOI in the InAs nanosheet is dominantly of Rashba type. However, all kinds of SOIs including e.g., Rashba type, Dresselhaus type, and other high-order types, in the nanosheet would contribute to spin relaxation rate $\frac{1}{\tau_{SO}} \propto \frac{1}{L_{SO}^2}$ and thus affect L_{SO}. In this section, we describe how the Rashba SOI strengths in the InAs nanosheet of Device 1 are estimated and provide additional data for the results of simulations obtained at the constant conductance values of $G \sim 7e^2/h$ and $\sim 4e^2/h$.

The origin of the Rashba SOI is the presence of an effective out-of-plane electric field induced by structural inversion asymmetry in the InAs nanosheet. To the lowest-order approximation, the Rashba SOI can be described by the Hamiltonian of $H_R = r_R \boldsymbol{\sigma} \cdot \boldsymbol{k} \times \boldsymbol{E}$, where $\boldsymbol{\sigma}$, $\boldsymbol{k}$, and $\boldsymbol{E}$ are the Pauli spin matrices, wave vector, and out-of-plane electric field, respectively. The Rashba SOI strength can be conveniently characterized by the Rashba coupling constant $\alpha = r_R E$, where r_R is a material-specific, Fermi-level dependent prefactor and E is the average strength of the out-of-plane electric field $\boldsymbol{E}$ in the InAs nanosheet. The Rashba spin-orbit precession length is related to the Rashhba coupling constant α via $L_{SO}^R = \hbar^2/m^*\alpha$, with m^* being the electron effective mass. Because the total spin relaxation time rate can be written as $\frac{1}{\tau_{SO}} = \frac{1}{\tau_R} +$

$\cdots$, where $\frac{1}{\tau_R}$ is the term originated from the Rashba SOI, we can get $\frac{1}{L_{SO}^2} = \left(\frac{m^* r_R}{\hbar^2}\right)^2 E^2 + C_0$, where C_0 is a field-independent constant.

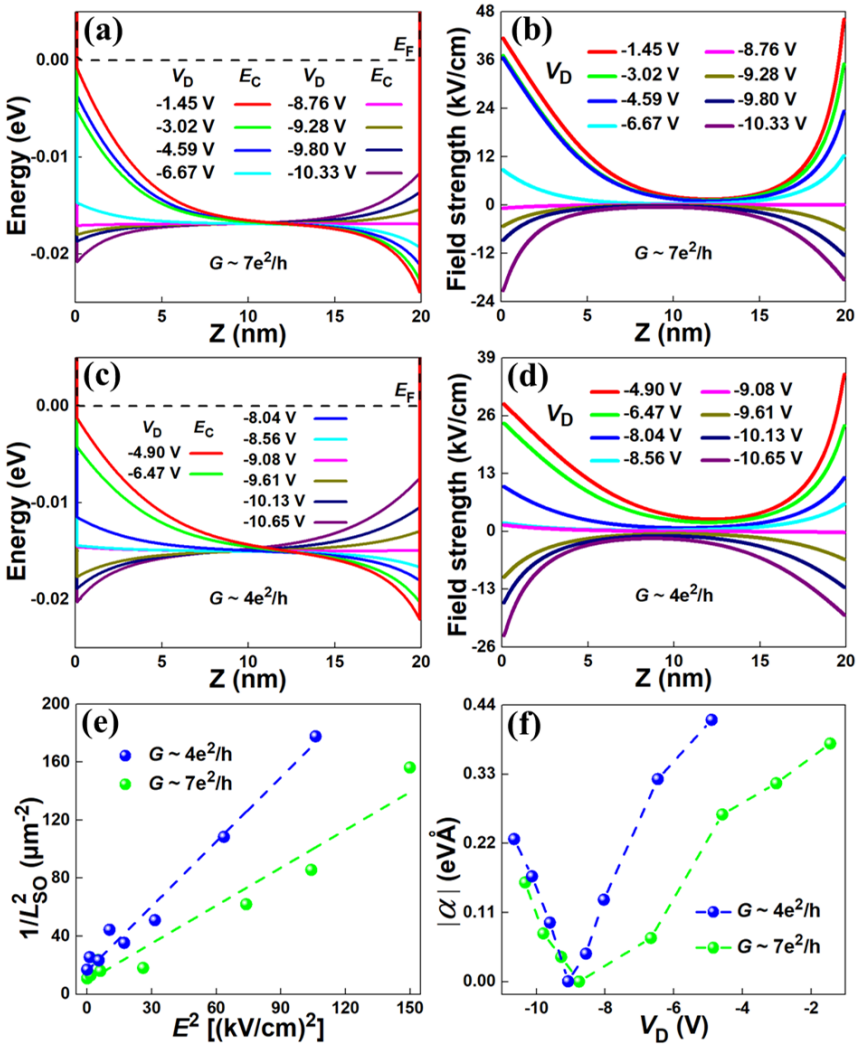

FIG. S5. (a) Simulated conduction band minimums E_C in the InAs nanosheet with a fixed value of $G \sim 7e^2/h$ (corresponding to $n \sim 1.07\times10^{12}$ cm^{-2} in the InAs nanosheet) for Device 1 at different dual-gate voltages V_D. (b) Electric field distributions in the InAs nanosheet derived from the simulated conduction band structures shown in (a). (c) and (d) The same as in (a) and (b), but for the device at $G \sim 4e^2/h$ (corresponding to $n \sim 5.8\times10^{11}$ cm^{-2} in the nanosheet). (e) Extracted $\frac{1}{L_{SO}^2}$ versus calculated E^2 in the InAs nanosheet. Here, E represents the average electric field strength in the nanosheet. Green and blue dots are the data points obtained at G~$7e^2/h$ and G~$4e^2/h$, respectively. The dashed lines are the linear fits to the data. (f) Estimated values of the Rashba spin-orbit coupling constant |α| in the InAs nanosheet of Device 1 at a few experimentally applied values of V_D.

Figures S5(a) and S5(c) show the simulated energy band diagrams in the InAs nanosheet of Device 1 at different applied V_D for the two fixed conductance values of $G \sim 7e^2/h$ and $\sim 4e^2/h$ (corresponding to $n \sim 1.07\times10^{12}$ cm^{-2} and $n \sim 5.8\times10^{11}$ cm^{-2} in the InAs nanosheet), respectively. Figures S5(b) and S5(d) show the corresponding effective out-of-plane electric field distributions in the InAs nanosheet, from which the average electric field strength E in the InAs nanosheet can be evaluated. It is seen that when the simulated conduction band E_C structures are tilted in the opposite ways, the evaluated electrical fields will point to opposite directions. To estimate the value of the Rashba coupling constant α, we plot the experimentally extracted $\frac{1}{L_{SO}^2}$ as a function of E^2 in Fig. S5(e). It is seen that $\frac{1}{L_{SO}^2}$ shows a good linear dependence on E^2 at both $G\sim7e^2/h$ and $G\sim4e^2/h$. From the slopes of the linear dependences, the prefactors $r_R\sim30.92$ e·nm^2 and $r_R\sim40.42$ e·nm^2 can be extracted for the nanosheet at the device conductance values of $G \sim 7e^2/h$ and $G \sim 4e^2/h$. Figure S5(f) shows the absolute values of the Rashba coupling constant $|\alpha|$ as a function of V_D for both conductance values. It is seen that $|\alpha|$ can be tuned from zero to a value of ~0.38 eVÅ at $G \sim 7e^2/h$, and from zero to a value of ~0.42 eVÅ at $G \sim 4e^2/h$. Thus, an efficient tuning of the Rashba coupling constant or the Rashba SOI strength in the InAs naonsheet with use of the dual gate has been demonstrated in our Device. Note that from the fits shown in Fig. S5(e), the values of C_0 could also be extracted out as ~ 9μm^{-2} at $G \sim 7e^2/h$ and ~16 μm^{-2} at $G \sim 4e^2/h$. If we assume that the electric field-independent contribution to the spin procession originates dominantly from the Dresselhaus SOI in the InAs nanosheet, the Dresselhaus spin-orbit precession length can then be estimated as $L_{SO}^D \sim 0.33$ μm and $L_{SO}^D \sim 0.25$ μm in the nanosheet at $G\sim7e^2/h$ and $G\sim4e^2/h$, respectively.

Section VI. Electron transport measurement study of an additional dual-gate field-effect InAs nanosheet device (named as Device 2)

In this section, we present our measurement results obtained from Device 2, i.e., a similar dual-gate field-effect device made from another epitaxially grown InAs nanosheet and demonstrate that the device shows the same dual-gate voltage tunable magnetotransport characteristics as Device 1.

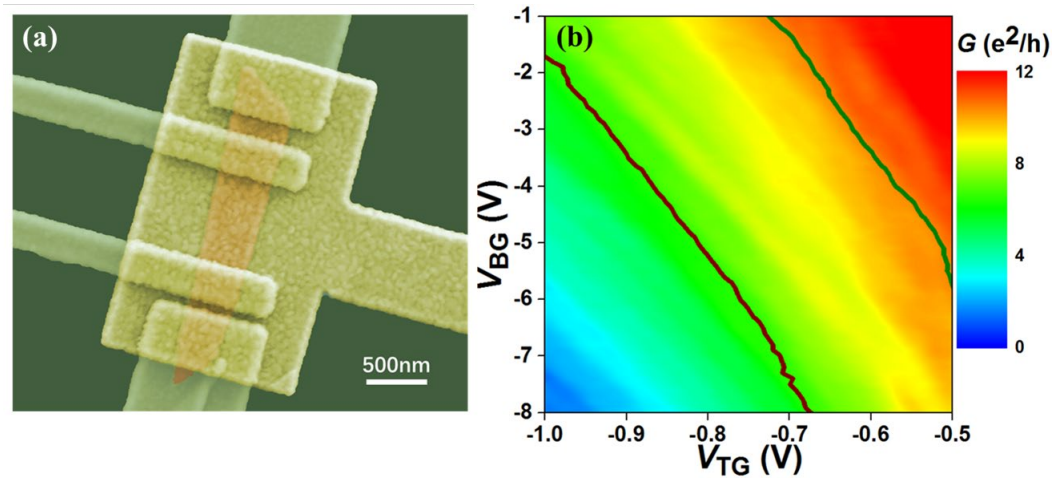

FIG. S6. (a) SEM image (top view, in false color) of Device 2, i.e., a dual-gate field-effect device with a similar device design as for Device 1 but made of another InAs nanosheet from the same MBE growth chip. (b) Conductance G of Device 2 measured in a four-probe setup [as shown in Fig. 1(c) of the main article] as a function of V_{BG} and V_{TG} at $T = 2$ K. The green and brown solid lines represent the constant conductance contours of $G \sim 10.4e^2/h$ and $G \sim 6.5e^2/h$, respectively.

Figure S6(a) displays an SEM image (top view, in false color) of Device 2. The layer structure of the device is the same as it shown schematically in Fig. 1(d) of the main article. The InAs nanosheet employed in Device 2 is grown by molecular beam epitaxy (MBE) and is in fact taken from the same growth chip as the InAs nanosheet used in Device 1. The measurements are performed in the same circuit setup as for Device 1.

Figure S6(b) shows the measured dual-gate transfer characteristics of Device 2 at a temperature of $T = 2$ K. It is again seen that both V_{BG} and V_{TG} can effectively tune the conductance G of the InAs nanosheet. The green and brown solid lines in Fig. S6(b) mark the constant conductance contours of $G \sim 10.4e^2/h$ and $G \sim 6.5e^2/h$, respectively.

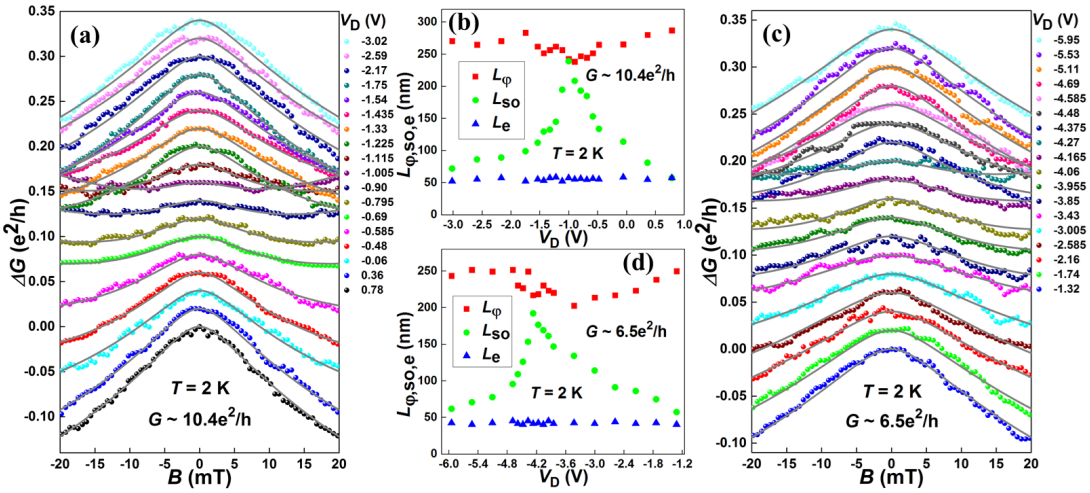

FIG. S7. (a) Low-field magnetoconductance ΔG measured for Device 2 at $T = 2$ K and at various dual-gate voltages V_D taken along the conductance contour of $G \sim 10.4e^2/h$. The bottom black data points display the measured ΔG data at $V_D = 0.78$ V and the ΔG data points measured at all other V_D values are successively vertically offset by $0.02e^2/h$ for clarity. The gray solid lines are the results of the fits of the measurements to the HLN theory [Eq. (1) in the main article]. (b) Characteristic transport lengths L_φ, L_{SO}, and L_e as a function of V_D extracted from the fits in (a). (c) The same as in (a) but for the dual-gate voltages V_D taken along the conductance contour of $G \sim 6.5e^2/h$. The bottom blue data points display the measured ΔG data at $V_D = -1.32$ V and the ΔG data measured at all other V_D values are successively vertically offset by $0.02e^2/h$ for clarity. Again, the gray solid lines are the results of the fits of the measurements to the HLN theory [Eq. (1) in the main article]. (d) Characteristic transport lengths L_φ, L_{SO}, and L_e as a function of V_D extracted from the fits in (c).

Figures S7(a) and S7(c) show the low-field magnetoconductance ΔG measured for Device 2 at $T = 2$ K and at different dual-gate voltages V_D (defined as $V_D = V_{BG} - V_{TG}$) taken along the conductance contours of $G \sim 10.4e^2/h$ and $G \sim 6.5e^2/h$, respectively. It is seen that the measured ΔG data at every V_D value display a peak-like structure near zero magnetic field, i.e., the WAL characteristics, indicating the presence of strong SOI in the InAs nanosheet. However, with decreasing V_D, the WAL peak feature is seen to become faint and then turn to get sharper and well-defined again in both the $G \sim 10.4e^2/h$ and the $G \sim 6.5e^2/h$ case. To extract characteristic transport lengths, the measured ΔG data are fitted to the HLN theory [Eq. (1) of the main article], see the

solid lines in Figs. S7(a) and S7(c) for the results of the fits. Figures S7(b) and S7(d) show the extracted values of L_φ, L_{SO}, and L_e as a function of V_D from the fits shown in Figs. S7(a) and S7(c), respectively. It is clearly seen that both L_φ and L_e exhibit a weak dependence on dual-gate voltage V_D. However, the extracted L_{SO} is modulated strongly by V_D in the same way as in Device 1, namely, with decreasing V_D, L_{SO} quickly increases to a peak value and then falls down quickly. This result demonstrates again that an SOI of the Rashba type is present in the InAs nanosheet in Device 2 and is greatly tunable with use of the dual gate. Note that when L_{SO} is tuned to its peak value by V_D, the Rashba SOI should vanish, and the remnant SOI is dual-gate voltage independent and could dominantly be of the Dresselhaus type arising from bulk inversion asymmetry in the nanosheet. Note also that the phase coherence length L_φ is comparably longer than the spin-orbit length L_{SO} over the entire tuning range of dual-gate voltages V_D in both the $G \sim 10.4e^2/h$ and the $G \sim 6.5e^2/h$ case. Thus, no crossover between L_φ and L_{SO} occurs with changing V_D. As a consequence, no WL characteristics should appear in the measured magnetoconductance of the InAs nanosheet, which is fully consistent with the measurement results shown in Figs. S7(a) and S7(c).

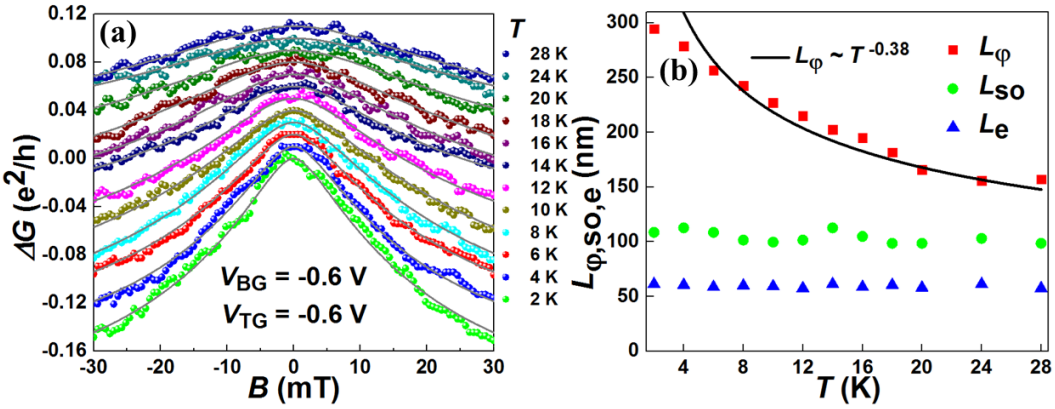

FIG. S8. (a) Low-field magnetoconductance ΔG measured for Device 2 at different temperatures T at fixed gate voltages $V_{BG} = –0.6$ V and $V_{TG} = –0.6$ V. The bottom green data points display the measured ΔG data at $T = 2$ K and the ΔG points measured at all other temperatures are successively vertically offset by $0.01e^2/h$ for clarity. The gray solid lines are the results of the fits of the measurements to the HLN theory [Eq. (1) in the main article]. (b) Characteristic transport lengths L_φ, L_{SO}, and L_e as a function of T extracted from the fits in (a). The black solid line is a power-law fit of the extracted L_φ, showing a $L_\varphi \sim T^{-0.38}$ temperature dependence.

Figure S8(a) shows the temperature-dependent measurements of the low-field magnetoconductance ΔG for Device 2 at fixed gate voltages $V_{BG} = -0.6$ V and $V_{TG} = -0.6$ V. Here, it is seen that all the measured ΔG data at temperatures ranging from 2 to 28 K show a peak-like structure near zero magnetic field, i.e., the WAL characteristics. Nevertheless, the WAL peak is sharp at $T = 2$ K and is gradually broadened with increasing T. Figure S8(b) shows the extracted L_φ, L_{SO} and L_e as a function of T from the fits of the measured data to the HLN theory [Eq. (1) in the main article]. It is seen that both L_{SO} and L_e show a weak temperature dependence, while L_φ decreases rapidly with increasing temperature. It is also found that the extracted L_φ in the InAs nanosheet can be fitted by a power-law temperature dependence of $T^{-0.38}$ [see the solid line in Fig. S8(b)]. This is the same result as found for Device 1 in the main article and again implies that the dephasing in the InAs nanosheet arises dominantly from electron-electron interactions with small energy transfers (the Nyquist scattering mechanism).